

Auto-calibration Method Using Stop Signs for Urban Autonomous Driving Applications

*Yunhai Han¹, *Yuhan Liu¹, David Paz¹, Henrik Christensen¹

Abstract—For use of cameras on an intelligent vehicle, driving over a major bump could challenge the calibration. It is then of interest to do dynamic calibration. What structures can be used for calibration? How about using traffic signs that you recognize? In this paper an approach is presented for dynamic camera calibration based on recognition of stop signs. The detection is performed based on convolutional neural networks (CNNs). A recognized sign is modeled as a polygon and matched to a model. Parameters are tracked over time. Experimental results show clear convergence and improved performance for the calibration.

I. INTRODUCTION

Recently, the expectations placed on autonomous driving have risen sharply, and many big companies and start-ups have launched their own production lines with different architectures. The needs of safe and comfortable driving give the advanced driver assistance systems (ADAS) an essential role in the development. Among all kinds of sensors supporting ADAS, the camera stands out for its low-cost and capability of capturing the scenarios with rich contexts. A camera system is frequently used in distance perception, speed inference, and object detection [1]. For these applications, the camera calibration parameters are often essential to reconstruct parts of a scene and can influence the accuracy of the measurements.

One can calibrate a camera once before the beginning of a task that requires minimal camera motion, as the intrinsic parameters are reasonably assumed to be unchanged. However, when the camera is mounted on a vehicle, the camera intrinsic parameters turn out to vary due to the mechanical vibrations caused by the rough street surfaces, or temperature fluctuations caused by the weather [2], [3], [4]. It is inconvenient to repeatedly calibrate a camera for a long-term application, and not practical throwing the technical task to an innocent customer, with the goal of popularizing autonomous vehicles. The long-term operations and the maintenance-free advantages of a camera system can only be guaranteed by auto-calibration methods, which can update the camera parameters continuously.

The commonly used camera calibration methods (e.g. [5]) require some special reference patterns, a chessboard, for example, whose physical size is known beforehand. However, these special patterns are not available when the vehicle is on the road. In this case, the auto-calibration system is necessary to extract the reference information from its environment.

*Equal contributions.

¹Contextual Robotics Institute, University of California, San Diego (UCSD), 9500 Gilman Dr, La Jolla, CA, 92093



Fig. 1: Example image showing a stop sign. The image is captured when the autonomous vehicle is driving around the UCSD campus.

There are a few auto/self-calibration methods proposed. Ribeiro [6], Hai [7], and Lu [8] extracts feature points from the road lines for calibration purpose, yet it is doubtful to assume the same width of the road lines in different regions. Also, because of frequent friction (with wheels), imperfections exist along the contours of road lines. These artifacts and variations can lead to undesirable calibration errors. In [9], two solutions are presented. One designs a structured environment (a grid of known size painted on the road) that the cameras detect as the vehicle drives near, the other puts several markers on the vehicle's hood, which may distract the drivers. Also, the hood is curved in most cases and is assumed to be within the FOV of the camera. Both are not suitable for real driving scenarios.

Stop signs, unlike a designed pattern, are ubiquitous (Fig. 1). The physical size of stop signs are standardized by the U.S. Department of Transportation [10].

Compared with other reference information existing in the urban environments, there are three advantages of using a stop sign:

- There are a number of adequate feature points that can be detected with sub-pixel accuracy (at least eight from the inner octagon corners of the stop sign).
- Compared with other reference objects (e.g., road lines), the relative geometric properties of a stop sign remain unchanged anywhere anytime, because they are made of metals which are resistant to external forces.
- A vehicle slows down when approaching a stop sign, reducing the image blurs and the rolling shutter effects.

Therefore, we present an approach to auto-calibrate with stop signs. The rest of the paper is organized as follows: Section II gives a brief summary of the related work; Section III

presents the details of our approach; Section IV shows the experiment results on the videos collected from the UCSD campus using four vehicular cameras.

II. RELATED WORK

Camera Calibration: Camera parameters can be estimated from enough pairs of 3D object points and corresponding 2D image points [11]. In [12], Zhang proposed to calibrate a camera with a planar object, opening the door to the famous chessboard calibration method [13].

Auto-calibration: Several researchers have also contributed to the auto-calibration using different reference objects. In [6][7][8], vanishing points or road corners were extracted from the dotted road lines for online calibration. In [14], predefined feature points from other automobiles were used to build the correspondence model, applied to obtain traffic camera parameters. In [15], surveillance camera calibration was based on three vanishing points defining the stream of vehicles. In [16], the same work was done through representing a walking human as a vertical line segment. Besides, [9] placed markers on the vehicle's hood, from which the relative positions and orientations of the on-board cameras can be estimated quickly.

Traffic Sign Detection: Object detection has been a well-studied area with the help of convolutional neural networks (CNNs). Proposal-free architectures (e.g. YOLO [17], YOLOv3 [18]) can easily run in real-time frequency of 45Hz, while proposal-based ones (e.g. Faster R-CNN [19], FPN [20]), though requiring more resources and typically taking longer to run, generally outperform the formers in terms of accuracy, especially with small objects and complicated scenes. As to tackle a related task, the instance segmentation method in [21], which labels the object pixels, can also be applied to find the stop sign bounding boxes. Besides, optimized architectures (e.g. [22], [23]) tailored for the traffic sign detection have been proposed as well.

Shape Matching: Shape matching checks the resemblance of two shapes using some similarity measure, or a metric [24]. Particularly in our case, the shape enclosed by the detected stop sign edges has to be an octagon. Arkin et al. [25] represented the polygons with the turning functions and measured the L_p distances. Huttenlocher and Kedem [26] moved further by considering (in addition to rotation, translation, and scale invariance) the affine invariance, with a Hausdorff distance on top of the normalized affine arc length representation of the polygon vertices. Later, several algorithms (e.g. [27], [28]) were introduced to speed up the calculation of the Hausdorff distance.

III. METHODOLOGY

The automatic system can be divided into seven modules (see Fig. 2).

The first five parts generate the 2D-3D correspondence pairs of corner points from an urban video or image sequence, followed by the last two steps calculating the intrinsic parameters.

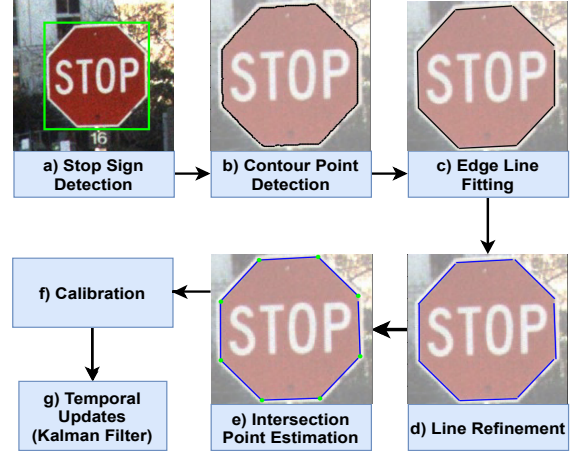


Fig. 2: A demonstration of the system framework. (a) The bounding box that contains the stop sign detected by Mask R-CNN. (b) The contour points (black dots) of the inner octagon obtained by the Canny/Deverny algorithm. (c)-(d) The estimated lines/edges. The black solid lines and the blue solid lines represent the estimated lines before and after line refinement, respectively. (e). The intersection/corner points. The green circles are the estimated intersections. The eight corner points are then used for homography estimation together with reference information.

A. Stop Sign Detection

A Mask R-CNN model with a ResNet-50 and Feature Pyramid Network backbone [29] were used to generate 2D bounding boxes on the image frames (see Fig. 2(a)). The network was pre-trained on COCO2017 [30].

B. Contour Points Detection through Color Segmentation

This module detects the contour points of the red inner octagon from a stop sign (Fig. 2(b)). An image pre-processing of color space conversion (from RGB to HSV) proves to be beneficial for the red color extraction with a threshold. Afterwards, the Canny/Deverny algorithm is used to attain the contour points of the octagon with sub-pixel accuracy:

a. The Canny Algorithm

Canny [31] applies the first derivative of a Gaussian filter over an image to get the image gradient, of which the edge points are the local maxima along the normal direction \mathbf{n} . The direction \mathbf{n} orthogonal to an edge can be approximated with the image gradient:

$$\mathbf{n} \approx \frac{\nabla(G \star I)}{|\nabla(G \star I)|}, \quad (1)$$

where G and I are the Gaussian filter and the image, respectively, and \star stands for the convolution operator.

b. The Deverny Sub-Pixel Correction

Edge points are attained with pixel precision through the Canny Algorithm, yet sub-pixel accuracy is desired in our system. This is where the Deverny Correction [32] comes as an improvement of the former. Suppose B is a pixel point obtained with the Canny Algorithm (a local gradient maximum in the corresponding normal direction \mathbf{n}). The gradients of two neighbouring points

of B along \mathbf{n} can be approximated through linear interpolation. Then, the sub-pixel position of the edge point is refined to the maximum of a 1D quadratic interpolation (along \mathbf{n}) of all these three points.

c. Contour Points Chaining

The above independent points can be grouped to form several chains [33], among which the one contains the most points is selected as the contour of the inner octagon, assuming a dense point detection (otherwise, the contour may be broken up into several pieces).

C. Edge Line Fitting

Given the set of 2D points $\mathbf{X} \in \mathbb{R}^{N \times 2}$ on the stop sign contour from above, eight lines are to be fitted, with each estimating an edge of the octagon.

The edges are estimated one at a time, by finding the line with the most "support points". A contour point "supports" a line when the point-to-line distance is within a closeness threshold (in this work, the threshold is fixed to 0.5 px to assure a sub-pixel accurate estimation). This line selection is done by running a RANSAC algorithm over pairs of contour points (Algorithm 1).

Algorithm 1: Estimating Edge i

```

for  $k \in \{1, \dots, K\}$  do
    Randomly sample two contour points;
    Fit a line through them;
    Find and count the support points of the line
    above;
    Record the support points whenever the count is
    the highest so far;
end
Find the least square line of the recorded support
points.
Determine the two end points of the line segment
from the extrema of the recorded support points.

```

With $p \in [0, 1]$ probability that the final least square line is the most supported line, the number of iterations K can be calculated as [11]:

$$K = \frac{\log_2(1-p)}{\log_2(1-w^2)}, \quad (2)$$

where $w = \frac{1}{(8-i)^2}$, $i \in \{0, \dots, 7\}$ is the chance of selecting a point from the support set, assuming that there are few outliers in \mathbf{X} off the contour.

Once an edge has been fitted, all the support points should be removed from the original set, so that the same Algorithm 1 can be repeated to find a different edge.

D. Line Refinement with Perpendicular Search

Primitive points from section III-B can stray away from the contour due to misleading color segmentation in the HSV space caused by poor illumination. Line refinement is therefore necessary to adjust the shifted lines back to the edges through a local search.

The magnitude of an image gradient reveals the position of the octagon contour, where the color changes most abruptly in the neighborhood. Starting from an estimated line of section III-C, we search for the local maximal gradient along the perpendicular direction of the line, and rotate the line to align with it (Algorithm 2).

Algorithm 2: Refining Line i

```

Sample  $S$  points evenly from the line;
for each point do
    Search for the closest maximal gradient;
    Record the refined point;
end
Find the least square line of the  $S$  refined points.

```

In the case of under-/over-exposure, the gradient peak of an edge may disappear. Thus, a refinement boundary is introduced to cope with this. With the assumption that the refinement should be subtle, a line is only updated when more than half of the S refined points are within the boundary. The refinement boundary is parameterized with a percentage $B \in [0, 1]$, meaning that a refined point is at most $100B$ percent of the white border width away from the original position along the perpendicular direction. To estimate the white border width of a stop sign, we multiply the length of an estimated line segment from Algorithm 1 with the width-to-length ratio of an inner polygon edge documented in the traffic sign regulation.

E. Estimation of Intersection Points

There are, at most, $\binom{8}{2} = 28$ intersection points from the eight estimated lines, while only eight of them are valid octagon corners. A simple yet empirically effective approach would be to select the intersection points closest to the end points of the line segments. After this, any estimation with a corner count not equal to eight is dropped.

Sorting the corner points in, for example, a clock-wise order helps obtain the 2D-3D correspondence. Further, the first corner can always be set as the one to the upper-left of the character "S", for stop signs generally stand upright.

It is never too cautious to check the shape. Hausdorff distance method in [26] is adopted to guarantee that the final eight-point set forms an octagon under an affine transformation, which is, though two degrees-of-freedom less than the actual projective transformation, the best we can do without getting into the chicken-or-egg dilemma.

F. Calibration with Planar Objects

The pinhole camera model [34] is used. A 3D point (X, Y, Z) in the world coordinates is projected into an image as a pixel (u, v) . The following equation relates (u, v) to (X, Y, Z) :

$$s \begin{bmatrix} u \\ v \\ 1 \end{bmatrix} = \mathbf{A} \begin{bmatrix} \mathbf{r}_1 & \mathbf{r}_2 & \mathbf{r}_3 & \mathbf{t} \end{bmatrix} \begin{bmatrix} X \\ Y \\ Z \\ 1 \end{bmatrix}, \quad (3)$$

where s is an unknown scalar and $\mathbf{A} \in \mathbb{R}^{3 \times 3}$ is the camera intrinsic matrix. $\mathbf{r}_1, \mathbf{r}_2, \mathbf{r}_3$ are the columns of the rotation matrix, and \mathbf{t} is the translation vector. They are often called the camera extrinsic parameters, for their function of transforming a world coordinate point to the camera coordinate system.

If the 3D coordinate system is fixed on a planar object like a chessboard or a stop sign, the Z component in Equ. 3 is always zero, which leads to a simplified equation:

$$s \begin{bmatrix} u \\ v \\ 1 \end{bmatrix} = \mathbf{A} \begin{bmatrix} \mathbf{r}_1 & \mathbf{r}_2 & \mathbf{t} \end{bmatrix} \begin{bmatrix} X \\ Y \\ 1 \end{bmatrix}. \quad (4)$$

We use $\mathbf{M} = (X, Y, 1)^T$ and $\mathbf{m} = (u, v, 1)^T$ to represent the position of a point on the planar object and its position in the image, respectively. Their relationship is defined by a homography matrix \mathbf{H} :

$$s\mathbf{m} = \mathbf{H}\mathbf{M} \text{ with } \mathbf{H} = \mathbf{A} \begin{bmatrix} \mathbf{r}_1 & \mathbf{r}_2 & \mathbf{t} \end{bmatrix} \quad (5)$$

As is clear, \mathbf{H} is a 3×3 matrix up to a scale factor.

In [35][36], the homography matrix \mathbf{H} can be computed using $N \geq 4$ points. In our system, 8 corner points of a stop sign are detected.

Let's represent \mathbf{H} by $\mathbf{H} = \begin{bmatrix} \mathbf{h}_1 & \mathbf{h}_2 & \mathbf{h}_3 \end{bmatrix}$. From Equ. 5, we can get:

$$\begin{bmatrix} \mathbf{h}_1 & \mathbf{h}_2 & \mathbf{h}_3 \end{bmatrix} = \lambda \mathbf{A} \begin{bmatrix} \mathbf{r}_1 & \mathbf{r}_2 & \mathbf{t} \end{bmatrix} \text{ with } \lambda = \frac{1}{s} \quad (6)$$

Based on the knowledge that $\mathbf{r}_1, \mathbf{r}_2$ are orthonormal, we have:

$$\begin{aligned} \mathbf{h}_1^T \mathbf{A}^{-T} \mathbf{A}^{-1} \mathbf{h}_2 &= 0 \\ \mathbf{h}_1^T \mathbf{A}^{-T} \mathbf{A}^{-1} \mathbf{h}_1 &= \mathbf{h}_2^T \mathbf{A}^{-T} \mathbf{A}^{-1} \mathbf{h}_2 \end{aligned} \quad (7)$$

These are the two constraints needed for computing the intrinsic matrix \mathbf{A} .

The methods of solving the camera calibration problem and obtaining the closed-form solution are described in [12]. We refer interested readers to that paper for more information.

In our system, assuming that the principal point is fixed at the center of the image plane, only the focal lengths f_x and f_y are computed and iteratively updated as shown in the next section. For chessboard calibration, we also enforce this assumption for the purpose of comparison.

The closed-form solution can be refined through maximum likelihood inference: The original calibration is used as the initial guess for the nonlinear optimization problem, which can be solved with the Levenberg-Marquardt Algorithm as implemented in [37]. Currently, this part is not included in our system.

G. Temporal Updates of Calibration with a Kalman Filter

The objective is to integrate intrinsic parameters over time. It is reasonable to assume that the errors are due to additive Gaussian noises, thus we use a Kalman filter.

The prediction step is:

$$x_{t+1} = \mathbf{F}x_t + \mathbf{G}u_t + \epsilon, \quad (8)$$

where x_t, x_{t+1} are two (vectors of) intrinsic parameters estimated at different times. As there is no systematic manipulation over the intrinsic parameters, we can leave out the term $\mathbf{G}u_t$. If we believe that the intrinsic parameters are constant within a short period of estimation (which is a fundamental assumption of our research), \mathbf{F} will just be the identity matrix.

The update step is:

$$p_t = \bar{\mathbf{H}}x_t + \delta, \quad (9)$$

which explains "given the current estimated intrinsic parameters x_t , what might be the true estimation of these parameters p_t right now". For this, $\bar{\mathbf{H}}$ is again an identity matrix.

The process noise ϵ and the measurement noise δ are Gaussian random vectors with zero means. Their covariances are denoted by (diagonal) matrices $\mathbf{Q} = \mathbb{E}(\epsilon\epsilon^T)$, $\mathbf{R} = \mathbb{E}(\delta\delta^T)$, respectively. \mathbf{Q} specifies how much we think the intrinsic parameters change over time, which should be low for a short estimating period. \mathbf{R} determines how much noise there is in one estimation. Intuitively, this measurement noise ought to decrease from a high value as the process goes, because the more images are used, a more accurate calibration is expected.

IV. EXPERIMENTS

A. Description of the Experimental Autonomous Vehicle

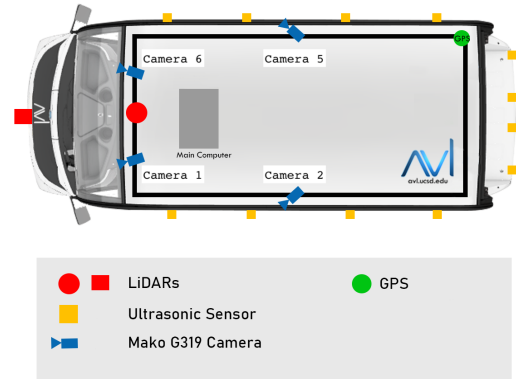


Fig. 3: Vehicle Sensor Configuration

Our experiment data was collected by one of our experimental autonomous vehicles. The vehicle is equipped with four cameras. The cameras are set up as two on the front and one on each side (Fig. 3). Videos of the cameras, data of LiDARs, and the vehicle positions were recorded for experiments, by driving along multiple routes around the UC San Diego campus [38]. The camera video was streamed at approximately 12Hz. The camera data are used for urban scenario experiments¹.

¹More information can be found on our website: <http://avl.ucsd.edu/>.

B. Datasets

The experiments were done using two datasets collected by the Autonomous Vehicle Lab (AVL). The video frames were stored in two different formats:

a. StopSignV1 - PNG Images Converted from Compressed JPG Images

Camera 1 and 5 detected 227 and 515 stop sign candidates from the video frames, respectively, and camera 6 detected 100 and 130 stop sign candidates at different times. The camera 2 images are too few to get a good calibration result, because stop signs are often found on the opposite side (right-hand side of the vehicle based on U.S. traffic rules). The ground-truth parameters (GT) were obtained from chessboard calibration before the video/image collection.

b. StopSignV2 - Uncompressed PNG Images

Only camera 5 and 6 were used, each detected 1507 and 1330 stop sign candidates, respectively. The ground-truth parameters (GT) were obtained from chessboard calibration beforehand.

C. Results

For scale-free comparison, the relative error ϵ_f of each parameter $f \in \{f_x, f_y\}$ is computed:

$$\epsilon_f = \frac{f - f^{GT}}{f^{GT}}, \quad (10)$$

where $f^{GT} \in \{f_x^{GT}, f_y^{GT}\}$ is the ground-truth intrinsic parameter.

a. StopSignV1 - Compressed PNG Images

For all of the four experiments, the refinement boundary percentages were the same: $B = 0.4$. Right before the calibration module, the system selected 98, 93, 66, and 93 good stop signs for experiments Camera1, Camera5, Camera6-Time1, and Camera6-Time2, respectively. We present both the tracked outputs of the complete system (red curves) and the pure calibration results (blue curves) as the number of image frames increases (Fig. 4 below and Fig. 9 in Appendix).

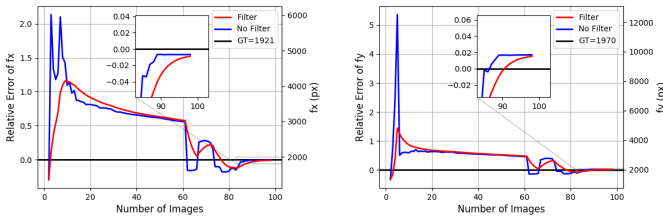


Fig. 4: Calibration Results of StopSignV1-Camera1 Data Using Kalman Filters

To show that the system can attain reasonable calibration parameters without the Kalman filter, for each camera dataset with N stop signs, we repeatedly remove one (different) stop sign at a time and calibrate using the remaining $N - 1$ stop signs. The mean relative error (number above each

column) and the corresponding standard deviation (red error bars) of these N calibrations are calculated (Fig. 5).

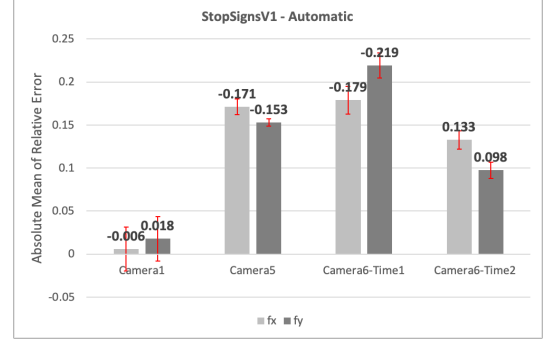


Fig. 5: Means and Standard Deviations of Relative Errors of StopSignV1 Calibration without Kalman Filters

The results of Camera5, Camera6-Time1, Camera6-Time2 can get even better (as shown in Fig. 6 below and 11 in Appendix) if no more than four stop signs are removed manually.

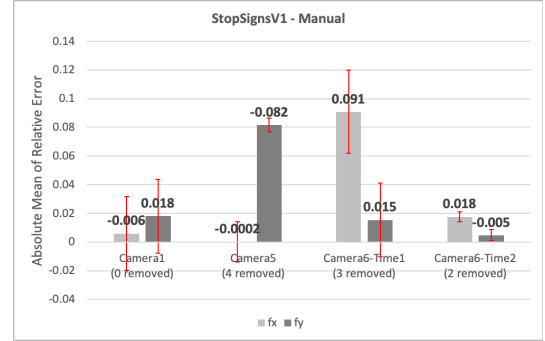


Fig. 6: Means and Standard Deviations of Relative Errors of StopSignV1 Calibration with Manual Stop Signs Removal

b. StopSignV2 - Uncompressed PNG Images

For all of the four experiments, the refinement boundary percentages were the same: $B = 0.0$ (i.e. no refinement). The system selected 444 (Camera5) and 844 (Camera6) good stop signs ready for calibration. System results with Kalman Filters are shown in Fig. 7 below and Fig. 10 in Appendix. The summary of pure calibration is Fig. 8.

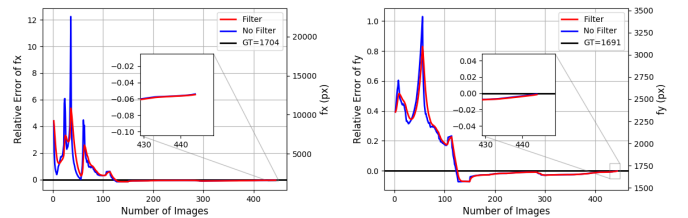


Fig. 7: Calibration Results of StopSignV2-Camera5 Data Using Kalman Filters

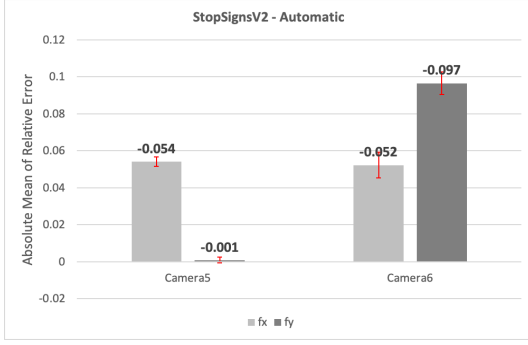


Fig. 8: Means and Standard Deviations of Relative Errors of StopSignV2 Calibration without Kalman Filters

D. Discussions

A 5% relative error is achieved for *StopSignV2*-Camera5 (Fig. 7), which has over 400 stop signs for calibration. If we consider the 1-2% variation of the chessboard calibration (which is verified by experiments), the above error can be as low as 3%. This is just 1% higher than that of the chessboard method.

Comparing Fig. 5 and 8, the automatic calibration results of *StopSignV2* are better than those of *StopSignV1*, for both camera 5 and 6. The reason is that more images were used in the calibration, the system will be more robust to some "bad matches" (e.g. the estimated lines deviate from the correct positions). Thus, the manual work is only useful when there are not many input images, which is rare in practice.

Notice that the uncompressed *StopSignV2* data should contain richer information than the compressed *StopSignV1*. However, experiments show that, when sliced into subsets of similar sizes as *StopSignV1*, the relative errors of *StopSignV2* are not significantly smaller than those of the former. It is, therefore, reasonable to conclude that for real applications, large number of images are preferred for accurate auto-calibration using our system.

E. Characterizing the Error

In this section, we present to the readers intuitively the effect of the relative error using a simple example of distance measurement. Suppose the principal point of a camera is fixed at the center of the image plane. A 3D point $P = (X, Y, Z)^T$ in the camera coordinates is projected to a pixel $p = (u, v)^T$ in the image plane. The pinhole camera model gives the relation:

$$Z = f_x \cdot \frac{X}{u} \quad \text{and} \quad Z = f_y \cdot \frac{Y}{v} \quad (11)$$

where f_x, f_y are the focal lengths estimated using our system. If an algorithm measures the object-to-camera distance Z from images captured by a camera calibrated using our system, the measurement error of Z (assuming the algorithm itself doesn't introduce any error) is equal to the relative error of the estimated focal lengths $\epsilon_{f_x}, \epsilon_{f_y}$. Take *StopSignV2*-Camera5 as an example (which achieved a 5% relative error), an object at 50m away will be estimated between 47.5 and

52.5m. This error range is acceptable for reacting safely in urban areas with a 25mph speed limit.

V. CONCLUSION

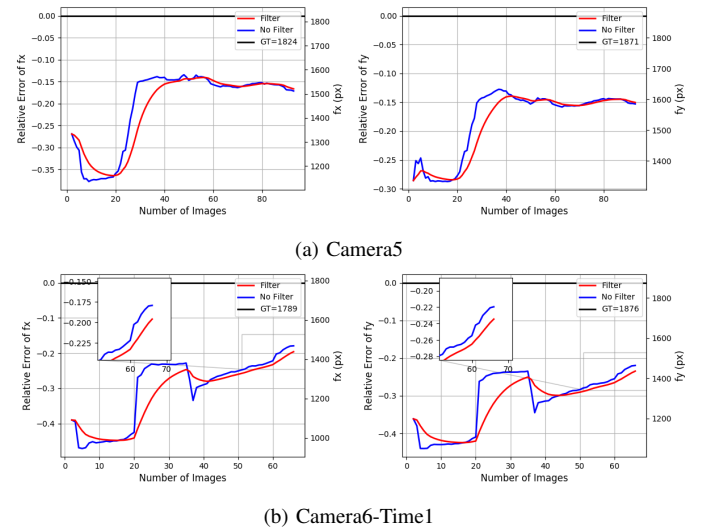
Our automatic system for intrinsic camera calibration using stop signs shows to have good performances in urban scenarios, with a convergence trend to solutions comparable with the chessboard calibration when the image number increases and a Kalman filter is applied. The system is more robust as the number of images is higher. The ability of continuously and accurately tracking the intrinsic parameters when driving on the road enables the long-term operations of a camera system for large-scale autonomous driving applications. It is also of interest to mention that chessboard calibration is more suitable to be considered as the baseline instead of the ground-truth. Experiments show that there were 1-2% variations in the chessboard calibration, which means the relative errors of our system may be smaller. In addition to the good performance, the system framework has the advantage of being easily adapted to using other traffic signs or landmarks. This allows us to create an auto-calibration toolbox, which will greatly benefit the whole autonomous driving community.

For future work, we will replace the HSV color space segmentation in the contour points detection with a better method (e.g. semantic segmentation), to improve the contour points detection at night. Also, we will introduce the Levenberg-Marquardt algorithm to refine the calibration results. Experiments will be carried out to compare the refined results with the current results.

ACKNOWLEDGMENT

Many thanks to Hengyuan Zhang for chessboard calibration, Andres Gutierrez for data pre-processing and all AVL lab members for the insightful discussions.

APPENDIX



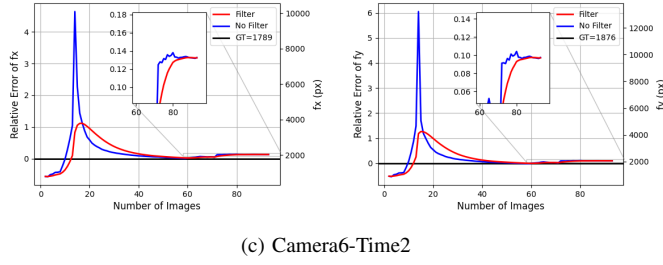


Fig. 9: Calibration Results of StopSignV1 Using Kalman Filters

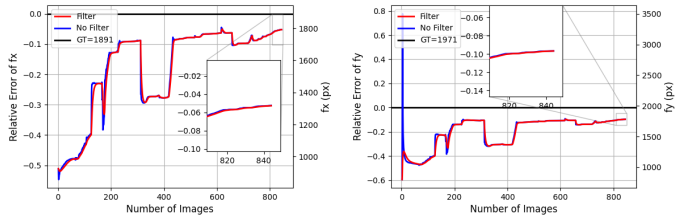


Fig. 10: Calibration Results of StopSignV2-Camera6 Data Using Kalman Filters

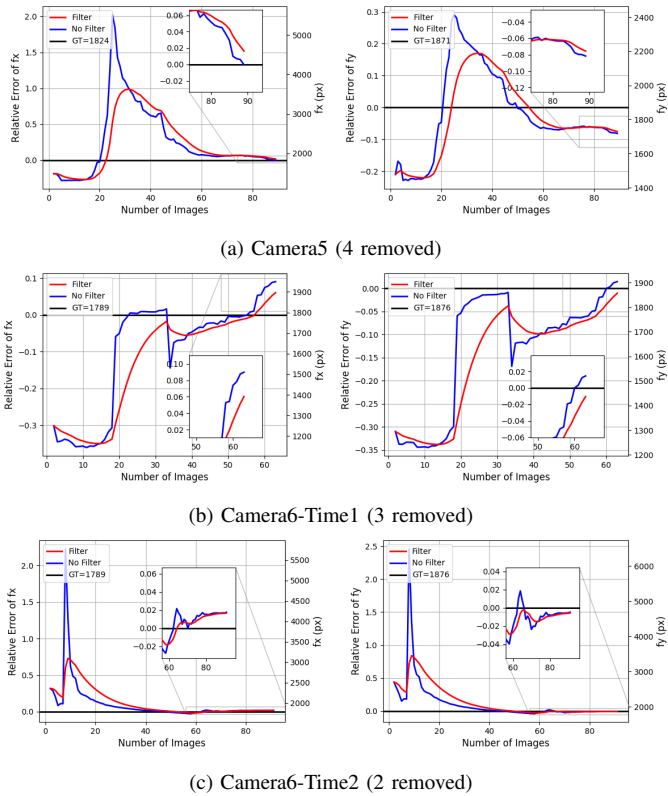


Fig. 11: Calibration Results of StopSignV1 Using Kalman Filters with Manual Stop Signs Removal

REFERENCES

- [1] A. Ziebinski, R. Cupek, H. Erdogan, and S. Waechter, "A survey of adas technologies for the future perspective of sensor fusion," in *Computational Collective Intelligence*, N. T. Nguyen, L. Iliadis, Y. Manolopoulos, and B. Trawiński, Eds. Cham: Springer International Publishing, 2016, pp. 135–146.
- [2] T. Dang, C. Hoffmann, and C. Stiller, "Continuous stereo self-calibration by camera parameter tracking," *IEEE Transactions on Image Processing*, vol. 18, pp. 1536–1550, 2009.
- [3] T. Låbe and W. Forstner, "Geometric stability of low-cost digital consumer cameras," *International Archives of Photogrammetry and Remote Sensing*, vol. 35, 01 2004.
- [4] M. Smith and E. Cope, "The effects of temperature variation on single-lens-reflex digital camera calibration parameters," *International Archives of the Photogrammetry, Remote Sensing and Spatial Information Sciences*, 05 2012.
- [5] J. Heikkilä and O. Silven, "A four-step camera calibration procedure with implicit image correction," in *Proceedings of IEEE Computer Society Conference on Computer Vision and Pattern Recognition*, 1997, pp. 1106–1112.
- [6] A. Ribeiro, L. Dohl, and C. Jung, "Automatic camera calibration for driver assistance systems," *International Conference on Systems, Signals and Image Processing*, 01 2006.
- [7] H. Wang, Y. Cai, G. Lin, and W. Zhang, "A novel method for camera external parameters online calibration using dotted road line," *Advanced Robotics*, vol. 28, 04 2014.
- [8] L. Lu, X. Lu, S. Ji, and C. Tong, "A traffic camera calibration method based on multi-rectangle," in *Intelligent Information Processing VII*. Berlin, Heidelberg: Springer Berlin Heidelberg, 2014, pp. 230–238.
- [9] A. Broggi, M. Bertozzi, and R. Fascioli, "Self-calibration of a stereo vision system for automotive applications," *Proceedings - IEEE International Conference on Robotics and Automation*, vol. 4, 03 2001.
- [10] (2003) Manual on uniform traffic control devices (mutcd). [Online]. Available: <https://mutcd.fhwa.dot.gov/HTM/2003r1/part2/part2b1.htm>
- [11] R. Hartley and A. Zisserman, *Camera Geometry and Single View Geometry*, 2nd ed. Cambridge University Press, 2004, p. 151–152.
- [12] Z. Zhang, "A flexible new technique for camera calibration," *IEEE Transactions on Pattern Analysis and Machine Intelligence*, vol. 22, no. 11, pp. 1330–1334, 2000.
- [13] A. Kaehler and G. Bradski, *Learning OpenCV 3: Computer Vision in C++ with the OpenCV Library*, 1st ed. O'Reilly Media, Inc., 2016.
- [14] R. Bhardwaj, G. Tummalam, G. Ramalingam, R. Ramjee, and P. Sinha, "Autocalib: Automatic traffic camera calibration at scale," *ACM Transactions on Sensor Networks*, vol. 14, pp. 1–27, 11 2018.
- [15] M. Dubska, J. Sochor, and A. Herout, "Automatic camera calibration for traffic understanding," *BMVC 2014 - Proceedings of the British Machine Vision Conference 2014*, 01 2014.
- [16] F. Lv, T. Zhao, and R. Nevatia, "Camera calibration from video of a walking human," *IEEE transactions on pattern analysis and machine intelligence*, vol. 28, pp. 1513–8, 10 2006.
- [17] J. Redmon, S. K. Divvala, R. B. Girshick, and A. Farhadi, "You only look once: Unified, real-time object detection," *CoRR*, vol. abs/1506.02640, 2015. [Online]. Available: <http://arxiv.org/abs/1506.02640>
- [18] J. Redmon and A. Farhadi, "Yolov3: An incremental improvement," *CoRR*, vol. abs/1804.02767, 2018. [Online]. Available: <http://arxiv.org/abs/1804.02767>
- [19] S. Ren, K. He, R. B. Girshick, and J. Sun, "Faster R-CNN: towards real-time object detection with region proposal networks," *CoRR*, vol. abs/1506.01497, 2015. [Online]. Available: <http://arxiv.org/abs/1506.01497>
- [20] T. Lin, P. Dollár, R. B. Girshick, K. He, B. Hariharan, and S. J. Belongie, "Feature pyramid networks for object detection," *CoRR*, vol. abs/1612.03144, 2016. [Online]. Available: <http://arxiv.org/abs/1612.03144>
- [21] K. He, G. Gkioxari, P. Dollár, and R. B. Girshick, "Mask R-CNN," *CoRR*, vol. abs/1703.06870, 2017. [Online]. Available: <http://arxiv.org/abs/1703.06870>
- [22] Y. Wu, Y. Liu, J. Li, H. Liu, and X. Hu, "Traffic sign detection based on convolutional neural networks," in *The 2013 International Joint Conference on Neural Networks (IJCNN)*, 08 2013, pp. 1–7.
- [23] Z. Zhu, D. Liang, S.-H. Zhang, X. Huang, B. Li, and S.-M. Hu, "Traffic-sign detection and classification in the wild," *2016 IEEE Conference on Computer Vision and Pattern Recognition (CVPR)*, pp. 2110–2118, 2016.

- [24] R. Veltkamp, "Shape matching: similarity measures and algorithms," *Proceedings International Conference on Shape Modeling and Applications*, pp. 188–197, 2001.
- [25] E. M. Arkin, L. P. Chew, D. P. Huttenlocher, K. Kedem, and J. S. B. Mitchell, "An efficiently computable metric for comparing polygonal shapes," *IEEE Transactions on Pattern Analysis and Machine Intelligence*, vol. 13, no. 3, pp. 209–216, 1991.
- [26] D. P. Huttenlocher and K. Kedem, "Computing the minimum hausdorff distance for point sets under translation," in *Proceedings of the Sixth Annual Symposium on Computational Geometry*, ser. SCG '90. New York, NY, USA: Association for Computing Machinery, 1990, p. 340–349. [Online]. Available: <https://doi.org/10.1145/98524.98599>
- [27] G. Rote, "Computing the minimum hausdorff distance between two point sets on a line under translation," *Information Processing Letters*, vol. 38, no. 3, pp. 123 – 127, 1991. [Online]. Available: <http://www.sciencedirect.com/science/article/pii/0020019091902338>
- [28] B. Li, Y. Shen, and B. Li, "A new algorithm for computing the minimum hausdorff distance between two point sets on a line under translation," *Information Processing Letters*, vol. 106, no. 2, pp. 52 – 58, 2008. [Online]. Available: <http://www.sciencedirect.com/science/article/pii/S0020019007002864>
- [29] Y. Wu, A. Kirillov, F. Massa, W.-Y. Lo, and R. Girshick, "Detectron2," <https://github.com/facebookresearch/detectron2>, 2019.
- [30] T. Lin, M. Maire, S. J. Belongie, L. D. Bourdev, R. B. Girshick, J. Hays, P. Perona, D. Ramanan, P. Dollár, and C. L. Zitnick, "Microsoft COCO: common objects in context," *CoRR*, vol. abs/1405.0312, 2014. [Online]. Available: <http://arxiv.org/abs/1405.0312>
- [31] J. Canny, "A computational approach to edge detection," *IEEE Transactions on Pattern Analysis and Machine Intelligence*, vol. PAMI-8, no. 6, pp. 679–698, 1986.
- [32] F. Devernay, "A non-maxima suppression method for edge detection with sub-pixel accuracy," *INRIA Research Report*, vol. 2724, 11 1995.
- [33] R. Grompone von Gioi and G. Randall, "A Sub-Pixel Edge Detector: an Implementation of the Canny/Devernay Algorithm," *Image Processing On Line*, vol. 7, pp. 347–372, 2017.
- [34] R. Szeliski, *Computer Vision: Algorithms and Applications*, 1st ed. Berlin, Heidelberg: Springer-Verlag, 2010.
- [35] R. I. Hartley, "Minimizing algebraic error in geometric estimation problems," in *Sixth International Conference on Computer Vision (IEEE Cat. No.98CH36271)*, 1998, pp. 469–476.
- [36] R. I. Hartley, "In defense of the eight-point algorithm," *IEEE Transactions on Pattern Analysis and Machine Intelligence*, vol. 19, no. 6, pp. 580–593, 1997.
- [37] J. J. Moré, "The levenberg-marquardt algorithm: Implementation and theory," in *Numerical Analysis*, G. A. Watson, Ed. Berlin, Heidelberg: Springer Berlin Heidelberg, 1978, pp. 105–116.
- [38] D. Paz, P.-J. Lai, S. Harish, H. Zhang, N. Chan, C. Hu, S. Binnani, and H. Christensen, "Lessons learned from deploying autonomous vehicles at uc san diego," *In Field and Service Robotics*, August 2019.